Matrix–fiber bond behavior in PBO FRCM composites: A fracture mechanics approach

T. D'Antino [a], C. Carloni [b,*], L.H. Sneed [c], C. Pellegrino [a]

[a] University of Padova, via Marzolo 9, Padova 35131, Italy
[b] University of Hartford, 200 Bloomfield Avenue, West Hartford, CT 06117, USA
[c] Missouri S&T, 1401 North Pine Street, Rolla, MO 65409, USA

Article history:
Received 7 June 2013
Received in revised form 17 January 2014
Accepted 21 January 2014

1. Introduction

Strengthening and rehabilitation of reinforced concrete (RC) structures with externally-bonded composite materials represent an effective alternative to new construction because they allow for an extension of the original service life and therefore prevent demolition of existing structures. In the last two decades fiber reinforced polymer (FRP) composites have been the most common type of composite used for structural applications. FRP comprises of continuous fibers (usually carbon, glass, or aramid) and a thermosetting (organic) resin, typically epoxy, as the matrix. Promising newly-developed types of matrix that potentially represent a valid, sustainable, and durable alternative to epoxy are the so-called inorganic matrices. Within the broad category of inorganic matrices, polymer-modified cement-based mortars have raised some interest in recent years. Composite materials that employ modified cement-based mortars are usually referred to as fiber-reinforced cementitious matrix (FRCM) composites. Alternative names have been proposed in the literature [1] that refer to different types of matrix or application. In FRCM composites, fibers are typically bundled, and the fiber pattern can be modified from unidirectional to bidirectional textile weaves or fabrics in an attempt to improve the bond characteristics. The limited available literature [1–23] reports that FRCM composites can be used effectively for strengthening and rehabilitation of RC structures. However, the weakness of FRCM–concrete joints appears to be at the matrix–fiber interface [18–23] rather than in the substrate or at the matrix–concrete interface, as is typically observed with FRP composites [24–38]. In FRP–concrete joints, it

* Corresponding author. Address: University of Hartford, 200 Bloomfield Avenue, Room UT 302 I, West Hartford, CT 06117, USA. Tel.: +1 860 768 4857; fax: +1 860 768 5198.

E-mail addresses: tommaso.dantino@dicea.unipd.it (T. D'Antino), carloni@hartford.edu (C. Carloni), sneedlh@mst.edu (L.H. Sneed), carlo.pellegrino@unipd.it (C. Pellegrino).

Nomenclature

E	elastic modulus obtained by the authors from tensile tests of the fiber net
g	global slip measured by the LVDTs and used to control the direct shear tests
L	length of the concrete prisms
n	number of longitudinal fiber bundles
P	applied load
s	slip between the fibers and the matrix
σ	normal stress in the longitudinal fiber bundle
b^*	nominal width of a single longitudinal fiber bundle
b_1	width of the bonded area
b_2	width of the fiber net
E_f	elastic modulus of the FRP reinforcement
f'_c	specified compressive strength of concrete
G_F	fracture energy associated with the matrix–fiber interface
G_F^{dis}	fracture energy associated with the matrix–fiber interface obtained as the area of the cohesive material law derived from the discrete procedure that employs the measured strains
G_F^i	fracture energy associated with the cohesive interface between the fibers and the internal layer of matrix
G_F^e	fracture energy associated with the cohesive interface between the fibers and the external layer of matrix
G_F^{fit}	fracture energy associated with the matrix–fiber interface obtained as the area of the cohesive material law derived from the fitted strain profile
$\bar{g}$	maximum prescribed global slip
l_{eff}	effective bond length
l_{eff}^{FRP}	effective bond length of the FRP–concrete interface
l_r	residual bonded length
ℓ	length of the bonded area
n_f	number of plies of FRP reinforcement
P^*	maximum (peak) applied load
P_{deb}	experimental load-carrying capacity of the matrix–fiber interface associated with debonding
P_f	applied load associated with friction after the entire composite has debonded
$\overline{P}_{deb}$	theoretical load-carrying capacity computed through the fracture energy G_F
$\overline{P}_{deb}^{dis}$	theoretical load-carrying capacity computed through the fracture energy G_F^{dis}
$\overline{P}_{deb}^{fit}$	theoretical load-carrying capacity computed through the fracture energy G_F^{fit}
$\overline{\overline{P}}_{deb}$	theoretical load-carrying capacity computed from the axial strain $\bar{\varepsilon}_{yy}$
s_f	slip corresponding to the complete debonding of the fibers from the matrix
t^*	average thickness of a single longitudinal fiber bundle
t_f	nominal thickness of one ply of FRP reinforcement
$(P_1–P_2)$	range of the applied load within which debonding initiates
$(g_1–g_2)$	range of the global slip corresponding to $(P_1–P_2)$
ε_{yy}	axial strain in the longitudinal fibers
$\bar{\varepsilon}_{yy}$	average axial strain in the longitudinal fibers at the beginning of the bonded area corresponding to the four points selected in the range $(P_1–P_2)$
$\bar{\varepsilon}_{yy}^{FRP}$	axial strain corresponding to the load-carrying capacity of the FRP–concrete interface
σ^*	ultimate stress in the longitudinal fiber bundle corresponding to P^*
τ_f	shear stress associated with friction
τ_{zy}^i	shear stress at the interface between the fibers and the internal layer of matrix
τ_{zy}^e	shear stress at the interface between the fibers and the external layer of matrix

is well-understood that interfacial crack propagation typically occurs within a thin layer of the substrate close to the FRP composite, and therefore the concrete mechanical and fracture properties and the surface treatment play a fundamental role in the evaluation of the strengthening performance. If the present and future investigations on FRCM–concrete joints confirm that interfacial debonding occurs within the composite, the substrate on which the composite is applied may not play a key role in the design of the strengthening system, which is an interesting aspect of this composite. Large slips at the interface between fibers and matrix have been observed during the debonding of FRCM composites from a concrete substrate. Further, the debonding process at the matrix–fiber interface is complicated by the *telescopic* behavior observed among the fiber filaments of a fiber bundle where the core filaments have a different mechanism of stress transfer with respect to the outer filaments, mainly due to the different impregnation of the fibers by the matrix [3,13]. FRCM composites are still in their

infancy, and a complete understanding of the interfacial stress-transfer mechanism is not available yet, although researchers have attempted a fracture mechanics approach to describe the behavior of the different filaments within the fiber bundle [3,13].

This paper presents an extensive experimental study that aims to describe the interfacial debonding of FRCM–concrete systems within the framework of fracture mechanics. As a first attempt to study the stress-transfer mechanism that characterizes FRCM composites, the macro-scale fracture mechanics approach used for FRP–concrete interfaces is extended in this paper to the matrix–fiber interface of FRCM composites.

2. Specimen preparation and test set-up

Eighty-two specimens, presented in this paper, were tested using the single-lap (direct) shear test set-up to study the bond characteristics of FRCM composites bonded to a concrete substrate. FRCM composite strips were externally bonded to concrete blocks (prisms). The classical push-pull configuration was adopted where the fibers were pulled while the concrete prism was restrained [21,22,27,30,37]. Two different concrete prisms were used, both of which had the same cross section (125 mm width × 125 mm depth), but different lengths (L = 375 mm or L = 510 mm). The faces of the concrete blocks

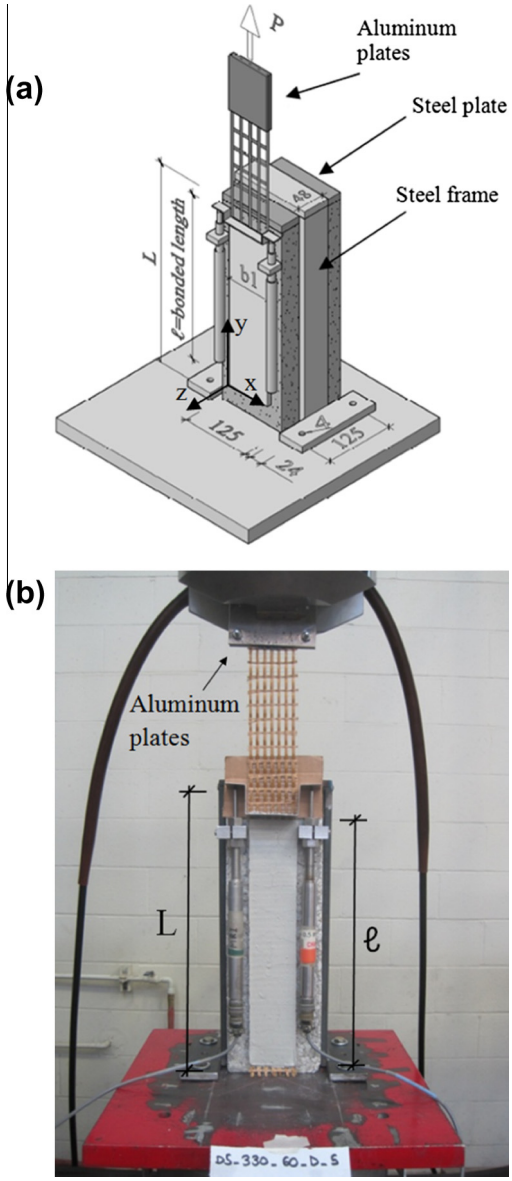

Fig. 1. (a) Test set-up. (b) Photo of specimen DS_330_60_D_5.

were sandblasted prior to applying the first (internal) layer of matrix. Only three faces of each block were used, corresponding to the three formed faces. The top face of the block, which was troweled smooth after casting, was disregarded. The composite material was comprised of bidirectional polyparaphenylene benzobisoxazole (PBO) fiber net and cementitious matrix. The nominal width b^* and average thickness t^* of one longitudinal fiber bundle were 5 mm and 0.092 mm, respectively. The matrix was applied only in the bonded area to embed the fibers and bond the composite to the concrete substrate (Fig. 1). The matrix was applied from the edge of the external longitudinal bundle on one side of the fiber strip to the edge of external longitudinal bundle on the other side of the fiber strip. Therefore, the width of the composite b_1 was equal to the width of the fiber net b_2 (Fig. 2a). Fibers were bare outside the bonded area. A 4 mm layer of matrix (internal layer) was applied using molds to control the composite width and thickness. A single layer of PBO fiber net was applied onto the matrix, and the fibers were pressed delicately onto the matrix to assure proper impregnation. The transversal fiber bundles, which were all on one side of the longitudinal fiber bundles, were placed against the internal layer of matrix for some specimens. A second (external) 4 mm layer of matrix was applied over the PBO fiber net. Thickness of the matrix layers was in accordance with the manufacturer's recommendations [39]. The bonded width (b_1) and length (ℓ) of the composite were varied. Two aluminum plates (Fig. 1a) were attached with a thermosetting epoxy to the end of the fiber strip to improve gripping during testing. For composite strips wider than 43 mm, the aluminum plates were also bolted together with four through-bolts at the plate corners to assure a uniform pressure on the gripped fibers and to prevent slippage of the fibers within the plates.

The concrete prism was restrained against movement by a steel frame bolted to the testing machine base. A steel plate was inserted between the steel frame and the top of the prism to distribute the pressure provided by the frame restraint. The direct shear tests were conducted under displacement control using a close-loop servo-hydraulic universal testing machine. Two linear variable displacement transducers (LVDTs) were mounted on the concrete surface close to the edge of the composite bonded region. The LVDTs reacted off of a thin aluminum Ω-shaped bent plate that was attached to the PBO transversal fiber bundle surface adjacent to the beginning of the bonded area as shown in Fig. 1a and 1b. The average of the two LVDT measurements is defined as the global slip g in this paper. Based on previous single-lap tests conducted on FRP–concrete joints [27,30,37], the global slip was increased at a constant rate of 0.00084 mm/s for all tests. The applied load is termed P in this paper (Fig. 1a).

3. Material properties

The concrete prisms were constructed with normalweight concrete with portland cement (Type 1) without admixtures. The maximum size of the aggregate was 9.5 mm. Twelve (6 + 6) 100 mm × 200 mm concrete cylinders were cast from the two batches of concrete used to construct the shorter (L = 375 mm) and longer (L = 510 mm) concrete blocks. The average compressive strength [40] and splitting tensile strength [41] were 42.5 MPa (CoV = 0.013) and 3.4 MPa (CoV = 0.113) for the shorter blocks, and 33.5 MPa (CoV = 0.085) and 3.0 MPa (CoV = 0.042) for the longer blocks. At least two 50 mm × 100 mm cylinders were cast from each batch of matrix used to cast the FRCM composite. The average compressive [40] and splitting tensile [41] strengths of the matrix were 28.4 MPa (CoV = 0.092) and 3.5 MPa (CoV = 0.231), respectively. The values determined from each batch were consistent, which indicates that the matrix was cast consistently throughout the batches. The compressive strength of the mortar is in good agreement with values provided in [1,39].

Seventeen tensile tests of the PBO fiber net were carried out to verify the efficacy of the gripping system prior to conducting the shear tests (Fig. 2a) and determine the mechanical properties of the fiber net. It should be pointed out that the testing procedure described in [42] was used even though the fibers were not impregnated with epoxy or mortar. Two aluminum

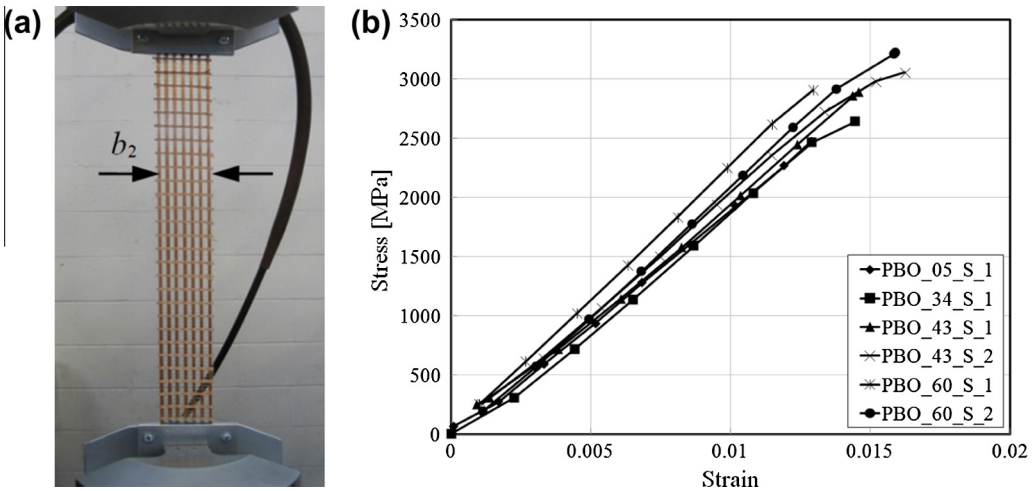

Fig. 2. (a) Photo of tensile test (specimen PBO_60_1). (b) Stress–strain relation of PBO fiber nets.

plates were attached to each end of the fiber net in the same manner as described for the direct shear tests. The tensile tests were performed on fiber nets of various widths (b_2) to determine if a width effect related to the gripping system occurred [22]. Strain gauges were mounted on the central fiber bundles of several specimens of various widths. Tensile specimens were named following the notation PBO_X_S_Z, where X = width b_2 of the fiber strip in mm, S (if present) indicates that strain gauges were mounted on the specimen, and Z = specimen number [22].

The stress–strain curves obtained from those specimens with strain gauges are plotted in Fig. 2b. The stress plotted in Fig. 2b was computed as the applied load P divided by the cross-sectional area of the longitudinal fiber bundles nb^*t^*, where n is the number of longitudinal bundles. The average measured tensile strength, ultimate strain, and elastic modulus E were 3014 MPa (CoV = 0.068), 0.0145 (CoV = 0.104), and 206 GPa (CoV = 0.065), respectively. The results of the tensile tests indicated that no width effect occurred among fiber nets of different widths. Thus, it was decided that the gripping system was effective and could be used for the direct shear tests. The results of the tensile tests will be plotted in Section 5 in an attempt to compare them with the direct shear test results. The ultimate strength, ultimate strain, and elastic modulus of the PBO fibers provided by the composite manufacturer were 5800 MPa, 0.025, and 270 GPa, respectively [39]. The tensile strength obtained from the tensile tests, although consistent, was substantially lower than the value reported by the manufacturer. The authors contacted the fiber manufacturer to gain information about the methodology used to conduct the tensile tests. Single yarns (bundles) were tested by the fiber manufacturer, and fibers were twisted to an optimized twist level prior to testing [43]. Given the different testing protocol used by the authors, a comparison between the results of the tensile tests performed on the fiber net and the values provided by the manufacturer was not attempted.

4. Applied load-global slip response

The direct shear test specimens were named following the notation DS_X_Y_S_D_Z^T, where X = bonded length (ℓ) in mm, Y = bonded width (b_1) in mm, S (if present) indicates strain gauges were mounted on the specimen, D (if present) denotes that the specimen was tested until the applied load P maintained a constant value, and Z = specimen number (Table 1). A superscript T after Z indicates that the fiber net was oriented with the transversal fiber bundles directly against the matrix internal layer. The peak load P^* and the number of longitudinal fiber bundles n, across the width of the composite, are provided in Table 1 for all specimens presented. The results of the tests presented in Table 1 suggest that the orientation of the transversal fibers did not significantly influence the peak load P^*. This aspect will be further investigated in a future publication when additional data will be available.

As friction among fiber filaments and between fibers and matrix has been reported in the literature for similar composites [3,13], specimens denoted with a "D" were tested until the entire softening branch of the load response was obtained in order to investigate the residual capacity of the interface related to friction. Specimens tested for this purpose had a relatively long bonded length, ℓ = 330 mm or 450 mm, with respect to the entire set of tests. Specimens denoted with D were only a small fraction of the entire set of tests due to the duration of the tests. The remaining specimens were tested to a prescribed value of the global slip $\bar{g}$ (when $\ell \leqslant 330\,mm$ typically $\bar{g} = 5mm$) corresponding to the descending branch of the load response.

The load responses of representative specimens DS_330_60_D_5, DS_330_80_D_1, and DS_450_60_D_1 are plotted in Fig. 3a. The same load responses are also plotted in Fig. 3b in terms of the normal stress defined by:

$$\sigma = \frac{P}{nb^*t^*} \tag{1}$$

Eq. (1) is used to normalize the applied load in order to compare the results of specimens with different bonded widths. The cross-sectional area of the fibers in the longitudinal direction nb^*t^* was used to normalize the applied load P because the load is transferred from the fibers to the matrix.

Fig. 3a and b are representative of the majority of the tests presented in this study in which debonding occurred at the matrix–fiber interface. For the sake of clarity it should be pointed out that seven specimens tested, not included in Table 1, failed prematurely because the fibers outside the bonded region reached the tensile strength in one or more bundles as a consequence of the non-uniform distribution of the force across the bundles. This phenomenon will be discussed in Section 5 and was observed in specimens DS_200_60_1, DS_330_34_3-6, DS_330_43_4, and DS_330_43_S_4.

Fig. 4a shows an idealized applied load-global slip response, put forward by the authors, by combining the information inferred from the load responses of the specimens herein presented and the experimental and analytical evidence available in the literature [3,13]. Although during single-lap tests the eccentricity between the composite and the concrete prism generates a mixed-mode loading that may influence the results, it has been shown [26] that the effect of the Mode-I component on FRP–concrete joints with a small loading angle can be neglected for long bonded lengths. For this reason, the failure observed in single-lap tests can be assumed to be a pure Mode II, provided that the composite has a relatively long bonded length. For this reason, a Mode-II interfacial crack propagation is assumed to occur at the matrix–fiber interface. The first part of the idealized $P - g$ response is represented by a linear branch (OA) associated with elastic behavior of the bond between the fibers and the matrix. After point A (Fig. 4a), the response starts to be nonlinear; the interface between the fibers and the matrix experiences some micro-damage, and the value of the applied load P increases until the onset of debonding at the matrix–fiber interface, which corresponds to point B in Fig. 4a. After point B, if the idealized P–g curve referred to

Table 1
Direct shear test specimens.

Specimen	n	P^* (kN)	σ^* (MPa)	Specimen	n	P^* (kN)	σ^* (MPa)
DS_100_34_1^T	4	1.92	1040	DS_330_60_4^T	7	6.50	2020
DS_100_34_2^T	4	0.97	530	DS_330_60_5^T	7	6.28	1950
DS_100_34_3^T	4	1.62	880	DS_330_60_6	7	7.01	2180
DS_100_60_1	7	3.69	1150	DS_330_80_1	9	8.47	2050
DS_100_60_2	7	3.83	1190	DS_330_80_2	9	8.84	2130
DS_100_60_3	7	3.77	1170	DS_330_80_3	9	8.28	2000
DS_150_34_1^T	4	2.22	1210	DS_450_34_1	4	3.77	2050
DS_150_34_2^T	4	1.55	840	DS_450_34_2	4	3.85	2090
DS_150_34_3^T	4	2.87	1560	DS_450_34_3	4	3.97	2160
DS_150_34_4^T	4	2.34	1270	DS_450_60_1	7	6.40	1990
DS_150_60_1	7	5.25	1630	DS_450_60_2	7	6.34	1970
DS_150_60_2	7	5.04	1570	DS_450_60_3	7	6.44	2000
DS_150_60_3	7	3.05	950	DS_450_60_4	7	5.77	1790
DS_200_34_1	4	3.05	1660	DS_450_60_5	7	6.51	2020
DS_200_34_2	4	2.52	1370	DS_450_60_6	7	6.79	2110
DS_200_34_3	4	3.44	1870	DS_450_60_7	7	6.65	2060
DS_200_60_2	7	5.66	1760	DS_450_80_1	9	8.62	2080
DS_200_60_3	7	5.44	1690	DS_450_80_2	9	9.07	2190
DS_200_60_4	7	6.58	2040	DS_450_80_3	9	9.32	2250
DS_250_34_1^T	4	2.61	1420	DS_450_80_4	9	8.86	2140
DS_250_34_2^T	4	2.11	1150	DS_450_80_5	9	10.04	2420
DS_250_34_3^T	4	2.82	1530	DS_330_60_D_1	7	8.29	2570
DS_250_34_4	4	3.21	1740	DS_330_60_D_2	7	7.12	2210
DS_250_34_5	4	2.89	1570	DS_330_60_D_3	7	6.56	2040
DS_250_34_6	4	3.61	1960	DS_330_60_D_4	7	5.24	1630
DS_250_60_1	7	6.68	2070	DS_330_60_D_5	7	6.69	2080
DS_250_60_2	7	6.17	1920	DS_330_80_D_1	9	8.90	2150
DS_250_60_3	7	5.70	1770	DS_330_80_D_2	9	8.68	2100
DS_330_34_1^T	4	3.00	1630	DS_330_80_D_3	9	8.90	2150
DS_330_34_2^T	4	3.51	1910	DS_330_80_D_4	9	8.42	2030
DS_330_34_7	4	4.07	2210	DS_330_80_D_5	9	8.58	2070
DS_330_34_8	4	4.02	2180	DS_450_60_D_1	7	7.01	2180
DS_330_34_9	4	3.44	1870	DS_450_60_D_2	7	6.67	2070
DS_330_43_1^T	5	4.43	1930	DS_450_60_D_3	7	7.33	2270
DS_330_43_2^T	5	5.25	2280	DS_330_43_S_1^T	5	4.48	1950
DS_330_43_3	5	5.27	2290	DS_330_43_S_2^T	5	5.12	2230
DS_330_43_5	5	4.79	2080	DS_330_43_S_3^T	5	3.03	1320
DS_330_43_6	5	5.09	2210	DS_330_43_S_5	5	4.03	1750
DS_330_60_1^T	7	7.05	2190	DS_330_60_S_1	7	6.30	1960
DS_330_60_2^T	7	6.56	2040	DS_330_60_S_2	7	7.31	2270
DS_330_60_3^T	7	6.06	1880	DS_450_60_S_1	7	6.63	2060

FRP–concrete joints, a self-similar stress-transfer mechanism [27,30,37] would shift along the bonded length, and the load would remain constant while the slip increases (dashed line in Fig. 4a). In FRCM composites friction between single fiber filaments and between fibers and matrix [3,13] occurs in that portion of the composite where the fibers have debonded. Consequently, an increase in the applied load after the debonding initiates (point B) is observed to point C. The applied load at point B is also referred to as the debonding load, P_{deb}, or the load-carrying capacity of the matrix–fiber interface. If it is assumed that friction depends only on the material characteristics and the contact area between the debonded fibers and the matrix, and it does not decrease with increasing slip, its contribution can be assumed to result in a linear increase in P with the increase of the debonded length. An effective bond length l_{eff}, i.e. the minimum length needed to develop the load-carrying capacity of the interface P_{deb}, if it exists, can be determined from the strain distribution along the longitudinal fibers for points of the load response between points B and C, provided that the contribution of friction is clearly identified. Further discussion on the effective bond length will be provided in the next sections, where the stress-transfer mechanism will be investigated.

The different stages of the stress-transfer mechanism for the various points of the load response depicted in Fig. 4a are shown in Fig. 4b. The residual bonded length l_r is defined as the actual length of the bonded area, i.e. $l_r = \ell$ between points O and B. Between points B and C the applied load increases due to friction until the debonding process reaches the end of the bonded area. At point C, the applied load reaches the maximum (or peak) load P^*, and the residual bonded length is equal to the effective bond length ($l_r = l_{eff}$) (Fig. 4b). After point C, the applied load starts to decrease because the bond mechanism is no longer fully established ($l_r < l_{eff}$). After point D, the curve's concavity changes, and the applied load reduces at increasing rate. At this stage the residual bonded length l_r is considerably reduced. It should be noted that in FRP–concrete joints, mixed-mode fracture propagation occurs at the unloaded end of the composite when $l_r < l_{eff}$ [35]. This aspect was not

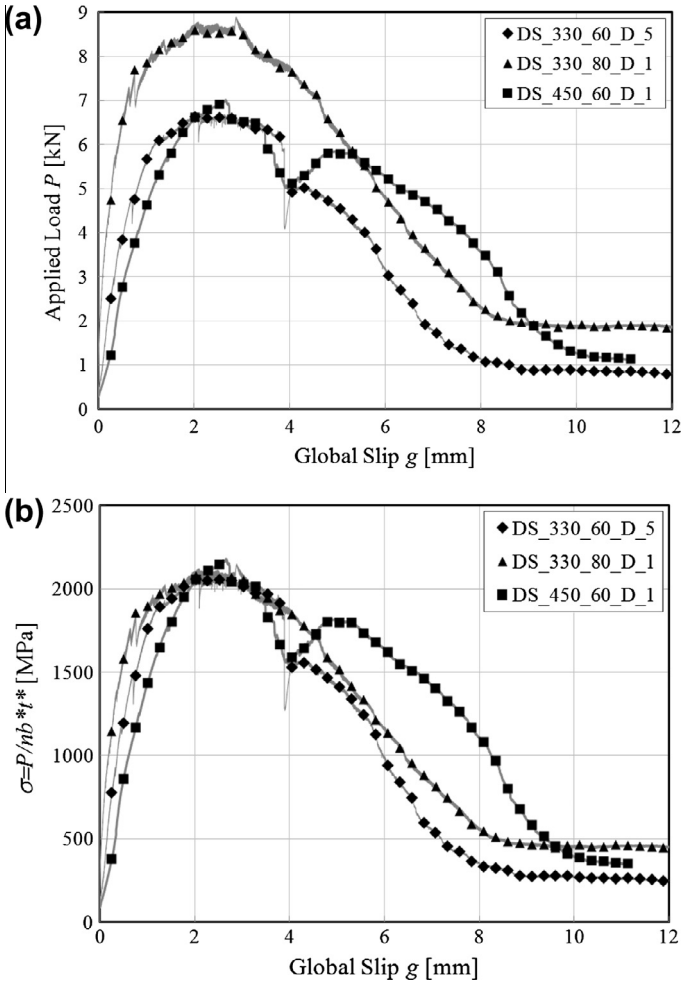

Fig. 3. (a) Applied load P vs. global slip g plot for specimens DS_330_60_D_5, DS_330_80_D_1, and DS_450_60_D_1. (b) Normal stress σ vs. global slip g plot for specimens DS_330_60_D_5, DS_330_80_D_1, and DS_450_60_D_1.

investigated in this work, and no measurements were attempted at the free end of the FRCM strip. At point E, the fibers are completely debonded from the matrix ($l_r = 0$), and the only residual contribution to the applied load is provided by friction. Thus, the load response becomes constant after point E with an applied load value associated with friction between single filaments and between fibers and matrix (P_f).

The shear stress τ_f associated with friction can be determined from the applied load at point E:

$$\tau_f = \frac{P_f}{2nb^*\ell} \tag{2}$$

where $nb^*\ell$ is the nominal bonded area of the longitudinal fiber bundles. The coefficient 2 takes into account that the contact area between fibers and matrix is twice the bonded area of the fiber bundles ($nb^*\ell$) because the fibers slip with respect to both layers of matrix (see also Fig. 9). Eq. (2) does not take into account the thickness t^* of the longitudinal fiber bundles in evaluating the contact area because the thickness t^* is much smaller than the width of the bundle, and its contribution to the contact area can be neglected. The average value of τ_f obtained from all specimens denoted with D was 0.06 MPa (CoV = 0.245).

The difference between the load at C, which corresponds to the peak load P^*, and the load at B, which corresponds to the debonding load P_{deb}, is related only to friction:

$$P^* - P_{deb} = 2\tau_f nb^*(\ell - l_{eff}) \tag{3}$$

where $nb^*(\ell - l_{eff})$ is the portion of the original bonded area in which the fiber bundles are subject to friction at point C ($l_r = l_{eff}$, see Fig. 4b).

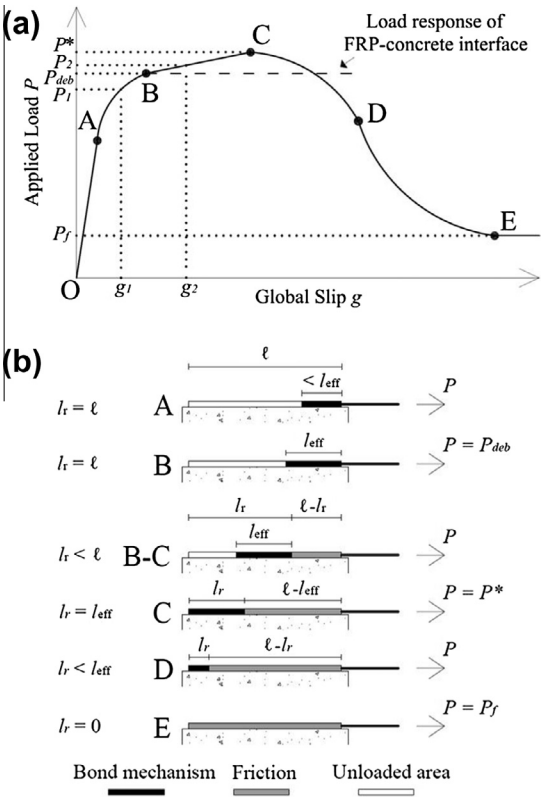

Fig. 4. (a) Idealized load P vs. global slip g response. (b) Stress–transfer mechanism stages corresponding to different points of the idealized $P - g$ response.

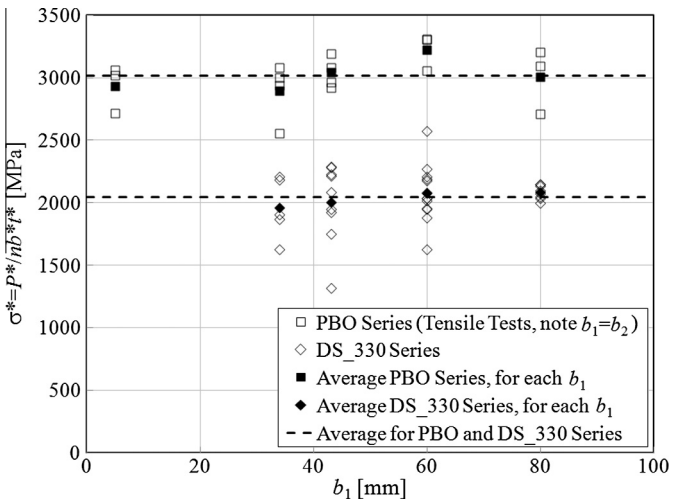

Fig. 5. Comparison of the ultimate stress σ^* vs. bonded width b_1 for single-lap shear tests (DS_330 Series) and tensile tests (PBO Series).

It should be pointed out that in the description of the idealized load response of Fig. 4a, the authors assumed that friction was present only after point B. However, a refined analysis should be carried out to identify the contribution and nature of friction that potentially occurs between fibers filaments, between the matrix and fibers, and between the longitudinal and transversal fiber bundles. The contribution of friction between fiber filaments and between the longitudinal and transversal fiber bundles before the onset of debonding is included in the macro-fracture model of the matrix–fiber interface presented in this paper.

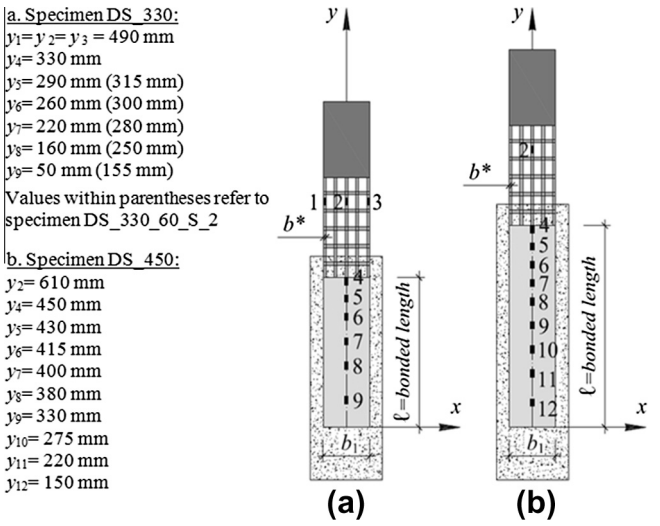

Fig. 6. Strain gauges positions for specimens in DS_330 Series (a) and DS_450 Series (b).

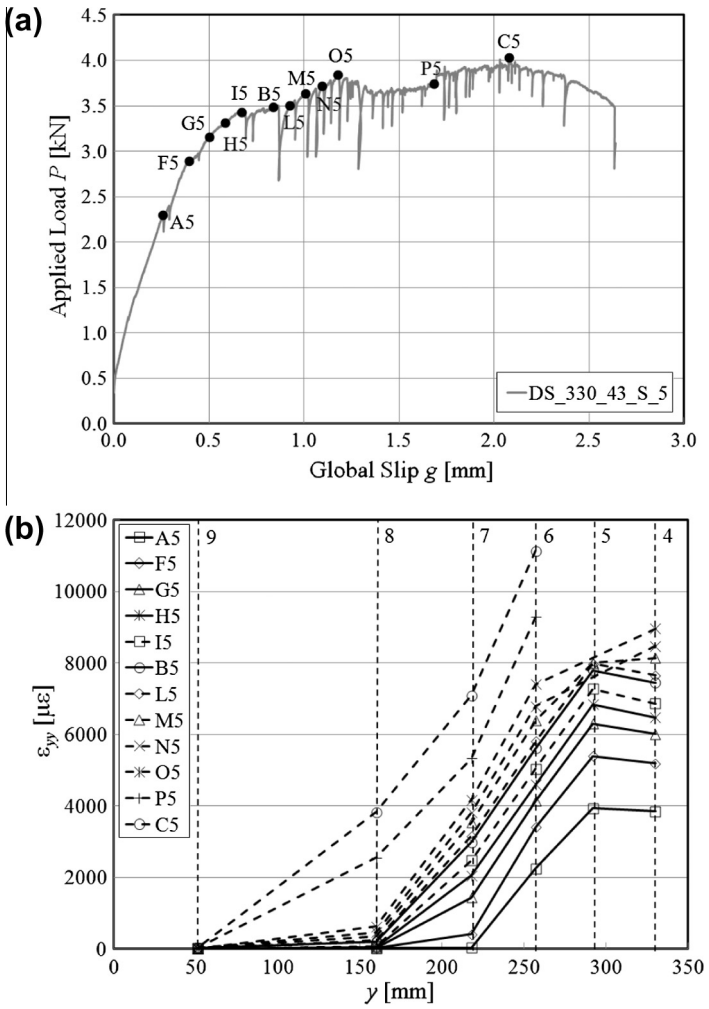

Fig. 7. (a) Applied load P vs. global slip g plot for specimen DS_330_43_S_5. (b) Axial strain ε_{yy} profiles along the bonded length for representative points of specimen DS_330_43_S_5.

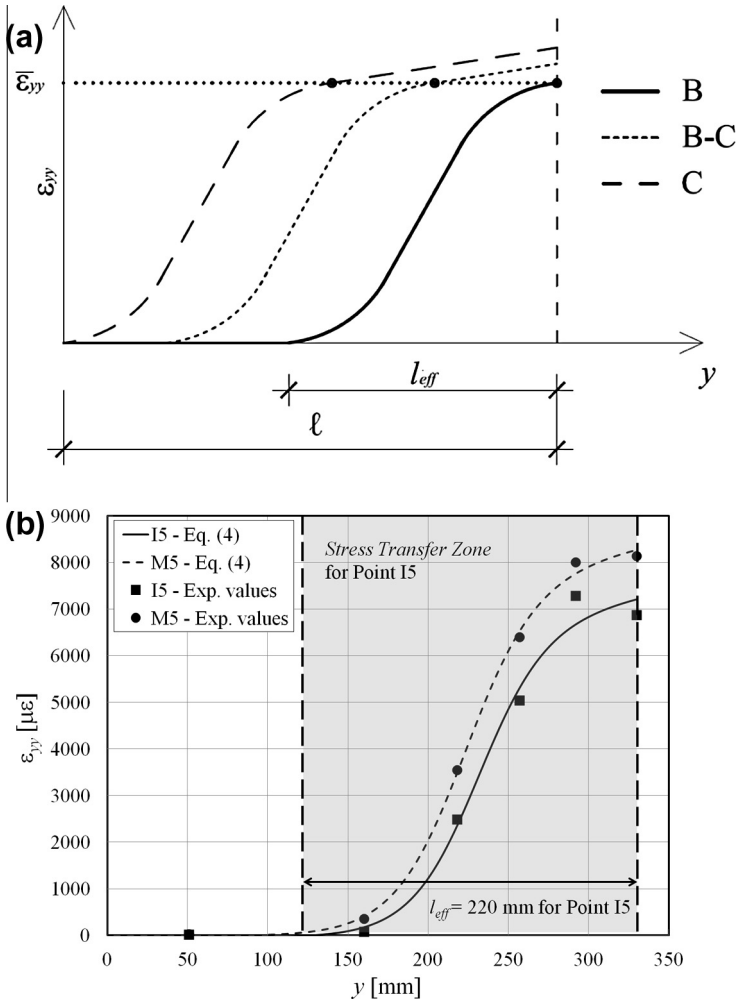

Fig. 8. (a) Idealized axial strain ε_{yy} profiles for points in Fig. 4a. (b) Fitting of the axial strain ε_{yy} profiles for points I5 and M5 of specimen DS_330_43_S_5 in Fig. 7a.

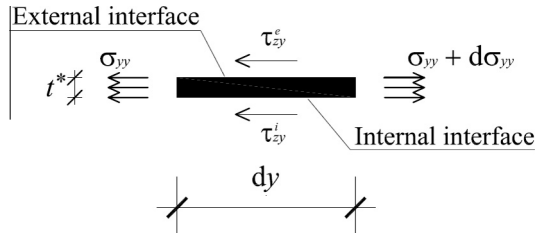

Fig. 9. Equilibrium of an infinitesimal segment of fibers embedded in the matrix.

5. Influence of the bonded width of composite

The ultimate stress σ^*, provided in Table 1, is computed from Eq. (1) using the peak load P^* in place of the applied load P ($\sigma^* = P^*/(nb^*t^*)$). Fig. 5 shows the results obtained in terms of σ^* for different composite bonded widths (b_1) for the test specimens with a bonded length ℓ = 330 mm (DS_330 Series). Specimens denoted with D and S were included in the plot of Fig. 5. The results, in terms of σ^*, of the fiber tensile tests (PBO Series) carried out by the authors are included for comparison. Four different composite bonded widths b_1 are shown (b_1 = 34 mm, 43 mm, 60 mm, and 80 mm). For each width of the DS_330

Series and the PBO Series, the average value of the ultimate stress is reported with a black filled marker. The average values of the ultimate stress for all tensile tests and all single-lap shear tests plotted in Fig. 5 are reported with dashed lines.

Pull-out tests of a single bundle of fibers indicated that failure of the fiber bundle is governed by the so-called *telescopic* behavior, i.e. the sequential failure of the fibers from the external sleeve to the internal core of the bundle [3]. This behavior is attributed to an uncontrolled variation in matrix impregnation between the fibers directly in contact with the matrix and those inside the bundle. Although it is possible that a width effect exists considering a single bundle of fibers, from Fig. 5 it can be concluded that a *global* width effect does not exist among multiple bundles and therefore for the entire width of the composite. The absence of a global width effect constitutes a unique characteristic of FRCM composites when compared to FRP composites [27,30,37]. It should be noted that, based on the experimental results presented (Fig. 5), a global width effect does not exist for FRCM–concrete joints with bonded width greater or equal to 34 mm. The absence of a global width effect for bonded width shorter than 34 mm cannot be confirmed by the experimental results.

The ratio between the average of the ultimate stress σ^* of the single-lap shear tests (2044 MPa) and of the fiber tensile tests (3014 MPa) is 0.68. This ratio should not be considered as an indication of the bond performance of the composite with respect to the tensile strength of the fiber net because the ultimate stress obtained from the single-lap shear tests is due not only to the bond but also to the friction between the fibers and between the matrix and the fibers that entails for an increase in the applied load once the debonding has initiated (see Eq. (3)).

The results obtained for bonded widths $b_1 = 34$ mm and $b_1 = 43$ mm show a larger scatter with respect to the other widths. This can be explained by the fact that the bundles placed at the edges of the composite are not completely surrounded by the matrix ($b_1 = b_2$), and therefore they are unable to develop the same bond capacity as the bundles inside the composite strip with matrix on each side. Moreover, the fact that the fibers are woven in discrete bundles can result in some of the bundles debonding before the others, leading to a non-uniform distribution of the load across the bonded width. An indication of the non-uniform distribution of the load among the bundles is provided by the difference between the measurements of the two LVDTs, which is the result of the rotation of the Ω-shaped bent plate attached to the transversal fibers. These two factors, namely the different impregnation of the bundles placed at the edges and the non-uniform distribution of the load across the width, are more emphasized for small bonded widths and become almost negligible as the bonded width increases.

6. Strain analysis

The results of seven specimens with different bonded widths and lengths and instrumented with strain gauges are presented in this paper. The geometrical characteristics of these specimens are listed in Table 1. The axial strain profiles presented in this section and the interfacial parameters determined in the next section refer to the Cartesian system shown in Figs. 1a and 6. Positions of the strain gauges along the bonded length are illustrated in Fig. 6 for specimens in series DS_330 and DS_450. It should be noted that positions of the strain gauges in specimen DS_330_60_S_2 were different from the other specimens with the same bonded length. For specimens DS_330_43_S_1 and DS_330_43_S_2, slots were created during the application of the matrix external layer, and the strain gauges were applied after the composite set. However, some concerns arose regarding possible stress concentration at the edges of the matrix slots. Hence, for the remaining specimens the strain gauges were applied directly to the bare fibers prior to applying the matrix.

To examine the load distribution among the different fiber bundles, the central and edge bundles of specimens DS_330_43_S_1 and DS_330_43_S_2 were instrumented with strain gauges in positions 1, 2, and 3 on the bare fibers [21,29]. Gauges 1 and 3 were omitted for the remaining specimens. The strain measured by gauges 1, 2, and 3 of specimens DS_330_43_S_1 and DS_330_43_S_2 was different for a given load level, confirming the non-uniform load distribution across the width of the composite [21,29]. This circumstance was also confirmed by the rigid rotation of the Ω-shaped bent plate.

Analysis of the axial strain on the surface of FRP composites bonded to concrete indicates that the zone in which the stress is transferred from the concrete substrate to the composite, the so-called stress transfer zone (STZ), is fully established for bonded lengths greater than the effective bond length when the load attains the value corresponding to debonding initiation. An increase of the global slip after initiation of the debonding process results in a simple translation of the STZ further along the bonded length of the composite while its shape remains constant [27,30,37]. Hence, the axial strain distribution along the FRP composite can be evaluated for any point of the load response after the onset of the debonding process. In FRCM composites, conversely, the presence of friction between single filaments and between fibers and matrix modifies the shape of the strain distribution at the loaded end once debonding has initiated. For this reason, the strain profiles of FRCM composites can be examined to determine the unique load value at which the bond mechanism is fully established and friction is not yet present (i.e. point B in Fig. 4a). If the strain profiles after point B are used to determine the STZ, the contribution of friction should be clearly identified in order to determine the fracture properties related to bond; otherwise they will be overestimated.

The point at which the stress-transfer mechanism is fully established and debonding starts to propagate (i.e. point B in Fig. 4a) is not easily determined from the experimental results. For this reason, the strain profiles corresponding to four points of the load response located in a small region around the assumed position of point B were considered. The range of load that defines the small region around point B and the corresponding range of g are named (P_1–P_2) and (g_1–g_2), respectively, and are illustrated in Fig. 4a. The region and the position of point B were identified a posteriori by the change in the slope of the load response, together with a sudden drop in the applied load caused by the formation of the debonding crack. Additionally, the choice of points used to analyze the strain profile is supported by the observation that for values of the

global slip g greater than those corresponding to the points used, the strain gauge closest to the loaded end, i.e. gauge number 4 in Fig. 6, showed a sudden increase in measured strain to values that were very large and almost constant. This can be interpreted as proof that the debonding process had initiated, since after that the mechanical interlocking provided by the matrix, which induced increasing shear stresses at the fiber-gauge interface, caused the debonding of the gauges from the fibers.

The load response of specimen DS_330_43_S_5 is shown in Fig. 7a. The strain profiles along the bonded length corresponding to the points indicated in Fig. 7a are shown in Fig. 7b. Points A5, B5, and C5 in Fig. 7a correspond to points A, B, and C in Fig. 4a, respectively. The vertical dashed lines in Fig. 7b are numbered according to the corresponding gauge (Fig. 6). Strain values from gauge 4 of specimen DS_330_43_S_5 are not reported in Fig. 7b for points P5 and C5, while strain values from gauge number 5 are not reported for points N5, O5, P5, and C5; strains measured in these positions were not consistent with the values recorded by gauges in the same position on other specimens or with values recorded by the closest gauges. This is likely due the onset of debonding which caused the detachment of the gauges. Interestingly, gauge 5 detached before gauge 4 probably due a different matrix–fiber bond condition along the longitudinal fibers.

The idealized axial strain profiles, put forward by the authors, corresponding to three points of the load response of Fig. 4a are illustrated in Fig. 8a. The linear part of the strain profile close to the loaded end is related to friction, which causes a linear increase of the strain at the loaded end related to the debonded length ($\ell - l_r$) (Fig. 4b).

The strain profiles obtained from each specimen equipped with strain gauges were approximated using Eq. (4), which represents a modification of a function used for FRP–concrete joints [27,30,37] to take into account friction in the debonded area:

$$\varepsilon_{yy} = \varepsilon_0 + \frac{\alpha + ky}{1 + e^{-\frac{y-y_0}{\beta}}} \tag{4}$$

ε_0, α, β, and y_0 were determined using nonlinear regression analysis of the measured strains, while $k = 2\tau_f/Et^*$. The strain distribution obtained in this manner follows an "S" shape with a value nominally equal to zero toward the free end and a linear increasing value where the fibers debonded from the matrix at the loaded end. The fitting curves obtained from Eq. (4), and corresponding to points I5 and M5 for specimen DS_330_43_S_5, are shown in Fig. 8b. It should be noted that for specimen DS_330_43_S_5 the four points within the small region around point B (Fig. 4a) were identified as I5, B5, L5, and M5. Similarly to the FRP–concrete interface [27], the length needed to fully establish the stress transfer zone (STZ) and the bond mechanism, i.e. the effective bond length l_{eff}, can be defined as the distance between the two points of the strain distribution in which the derivative is equal to zero at the free end and the derivative is constant at the loaded end. The effective bond length for point I5 is shown in Fig. 8b. The average value of the effective bond length obtained from the four points within the small region around point B, the load range (P_1–P_2), and the global slip range (g_1–g_2) for each specimen equipped with strain gauges are reported in Table 2. The average value of l_{eff} for the seven specimens presented is 260 mm (CoV = 0.102).

It should be noted that the effective bond length in the case of the PBO FRCM composite is much longer than the effective bond length that typically characterizes the FRP–concrete interface [27,30,37]. The reason for this difference can be attributed to the different nature of the debonding mechanism that for the case of FRP composites takes place within the concrete substrate, whereas for PBO FRCM composites mainly develops between the matrix and the embedded fibers. For the FRP–concrete interface, the effective bond length and the fracture process are related to the fracture process zone of the concrete substrate. In FRCM–concrete joints macro-fracture of the matrix and particles of matrix attached on the fibers were not observed, which potentially indicates that, for the tests presented in this study, the interfacial crack propagation does not occur in a thin layer of matrix close to the fibers but rather is associated with the failure of the chemical and mechanical bond between matrix and fibers.

7. Fracture mechanics approach

As a first attempt to study the stress-transfer mechanism that characterizes FRCM composites, the macro-scale fracture mechanics approach used for the FRP–concrete interface was extended to the matrix–fiber interface of FRCM composites. The cohesive material law was obtained by combining the interfacial shear stress τ_{zy} with the corresponding slip s between

Table 2
Results obtained through the strain analysis and fracture mechanics approach for specimens instrumented with strain gauges.

Specimen	l_{eff} (mm)	(g_1–g_2) (mm)	(P_1–P_2) (kN)	P_{deb} (kN)	$\bar{\varepsilon}_{yy}$ (με)	G_F^{dis} (J/m^2)	G_F^{fit} (J/m^2)
DS_330_43_S_1^T	300	(1.7–2.3)	(3.90–4.11)	3.96	8760	360	450
DS_330_43_S_2^T	280	(1.5–1.8)	(3.98–4.39)	4.17	11020	630	680
DS_330_43_S_3^T	280	(1.2–1.5)	(2.63–2.72)	2.71	8200	350	240
DS_330_43_S_5	230	(0.7–1.0)	(3.42–3.64)	3.51	7770	270	300
DS_330_60_S_1	260	(0.9–1.2)	(5.51–5.91)	5.74	8920	350	360
DS_330_60_S_2	225	(0.7–0.9)	(6.49–6.75)	6.65	10420	480	550
DS_450_60_S_1	255	(1.1–1.3)	(5.50–5.91)	5.70	8970	420	540

the fibers and the matrix at the onset of the debonding process, i.e. point B in Fig. 4a. The strain profiles of four different points located around point B of Fig. 4a were considered, as discussed in Section 6. The free body diagram of an infinitesimal element of the fibers is depicted in Fig. 9.

Since the debonding occurs at the matrix–fiber interface, two interface surfaces, named interface *i* (internal) and interface *e* (external), must be considered that are associated with the shear stresses τ^i_{zy} and τ^e_{zy} (Fig. 9).

The role of the two interfaces will be discussed in a future publication by the authors where the results of specimens without the external layer of matrix will be presented. As a first attempt it will be assumed that the shear stresses at the internal and external interfaces are equal [18]. Consequently, the equilibrium condition yields:

$$\tau^i_{zy} = \tau^e_{zy} = \frac{1}{2} E t^* \frac{\mathrm{d}\varepsilon_{yy}}{\mathrm{d}y} \tag{5}$$

where E and t^* are the elastic modulus and the average thickness of the fibers, respectively. It should be noted that Eq. (5) is valid if: (i) a pure Mode-II loading condition is considered; (ii) the fiber strip is considered homogeneous and linear elastic until failure; and (iii) the thickness and width of the fibers is constant and variation along the length is neglected. If the matrix layers and concrete substrate are considered rigid, the slip $s(y)$ between the fibers and the matrix can be obtained from the integration of the axial strain ε_{yy} measured along the bonded length. The area under the curves $\tau^i_{zy} - s$ and $\tau^e_{zy} - s$ provides the value of the fracture energies of interfaces *i* (G^i_F) and *e* (G^e_F):

$$G_F = G^i_F = G^e_F = \int_0^{s_f} \tau^i_{zy} \mathrm{d}s = \int_0^{s_f} \tau^e_{zy} \mathrm{d}s \tag{6}$$

where s_f is the slip corresponding to the complete debonding of the fibers from the matrix. Eq. (6) implicitly entails that the slip between fibers and the two layers of matrix at the internal and external interfaces is the same, which is consistent with the assumption that the matrix is rigid. In addition, Eq. (6) entails that failure occurs simultaneously at interfaces *i* and *e*. The fracture energy G_F of Eq. (6) should be interpreted as an *average* energy. In fact, the strain of the fiber filaments varies within the fiber bundle, and strain gauge readings are averaged across the bundle [3,13]. In addition, the macro-scale approach used in this paper does not capture the complex phenomenon at the matrix–fiber interface where core filaments have a different degree of bond due to the limited impregnation by the matrix [3,13].

Fig. 10a shows the idealized τ_{zy}–s relationship which corresponds to the strain profiles of Fig. 8a. The fracture energy is the area under the curve in the range $0 \leqslant s \leqslant s_f$, without including friction [3].

Since the strain was measured at a limited number of points along the central bundle of the fiber strip, the accuracy of the τ_{zy}–s relationship and the fracture energy $G_F = G^i_F = G^e_F$ is affected by the procedure chosen to obtain the cohesive material law. In order to obtain a reliable value of the fracture parameters, as discussed in Section 6, four points around point B (Fig. 4a) were considered. In addition, two different procedures were utilized to obtain the cohesive material law and the associated fracture energy. The first procedure used the derivation and integration of the fitting function ε_{yy} (see Fig. 8b) provided in Eq. (4) to compute the shear stress τ_{zy} and the slip s. The second procedure consisted of the direct estimation of the derivative and integration of the strain profile in a discrete manner [29]:

$$\tau_{zy}(y_p) = \frac{1}{4} t^* E \left[(\varepsilon_{p-1} - \varepsilon_p)/(y_{p-1} - y_p) + (\varepsilon_p - \varepsilon_{p+1})/(y_p - y_{p+1}) \right] \tag{7}$$

$$s(y_p) = \sum_{q=p}^{N} \frac{1}{2} (\varepsilon_q + \varepsilon_{q+1})(y_q - y_{q+1}) \tag{8}$$

where y_p is the p-th strain gauge position, ε_p is the corresponding p-th strain gauge measurement, and $N = 9$ for $\ell = 330$ mm or $N = 12$ for $\ell = 450$ mm.

Fig. 10b shows the corresponding τ_{zy}–s curves obtained from the two procedures for points I5 and M5 of the load response of DS_330_43_S_5 depicted in Fig. 7a. The discrete τ_{zy}–s curves are affected by the limited number of points at which the axial strain was measured, and thus they differ from the fitting curves. The average values of the fracture energies obtained from the fitting (G^{fit}_F) and discrete (G^{dis}_F) procedures are reported in Table 2 for each specimen instrumented with strain gauges. The average values of G^{fit}_F and G^{dis}_F for each test were calculated from the same four points around point B used to determine the effective bond length l_{eff}.

The load-carrying capacity associated with initiation of debonding (point B) is related to the fracture energy according to Eq. (9) [25]:

$$\overline{P}_{deb} = nb^* \sqrt{4 G_F E t^*} = nb^* \sqrt{4 G^i_F E t^*} = nb^* \sqrt{4 G^e_F E t^*} \tag{9}$$

Eq. (9) is valid if a pure Mode-II interfacial loading condition occurs across the entire width and if $\tau^i_{zy} = \tau^e_{zy}$ holds (see Eq. (5)). As discussed in Section 5, although within the single bundle of fibers it is possible to recognize a width effect, a global width effect does not appear to exist for the entire width of the composite (Fig. 6). Hence Eq. (9) can be used to compute the

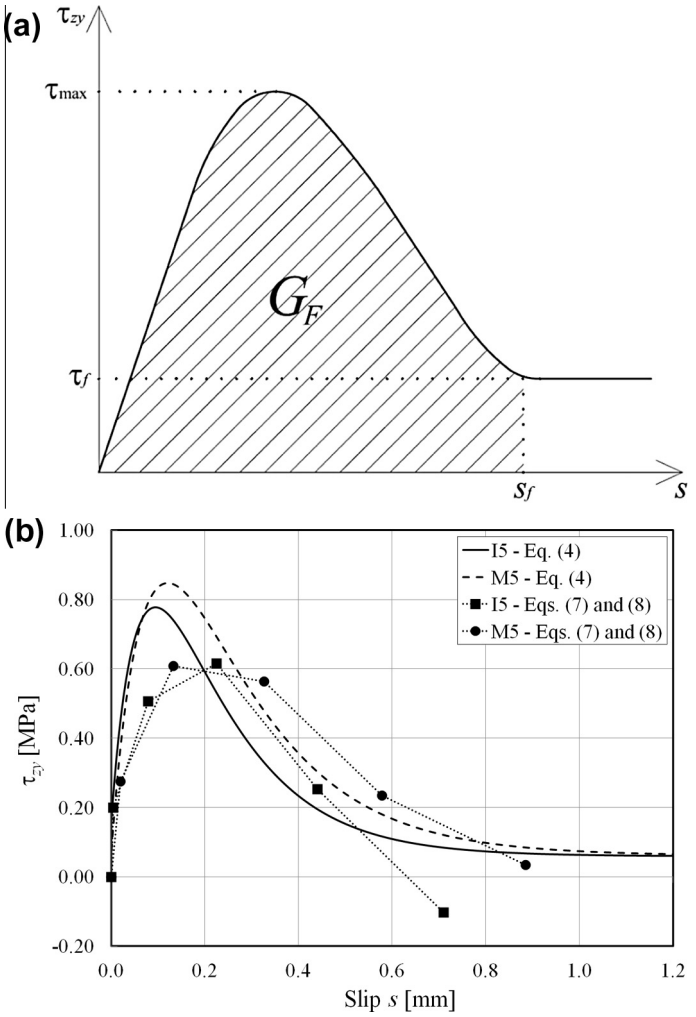

Fig. 10. (a) Idealized shear stress τ_{zy} vs. slip s curve. (b) Shear stress τ_{zy} vs. slip s curves for points I5 and M5 of specimen DS_330_43_S_5.

load-carrying capacity associated with initiation of debonding [33,37]. Note that Eq. (9) does not include friction, therefore $\overline{P}_{deb} \neq P^*$. The values of $\overline{P}_{deb}$ calculated from the fracture energies G_F^{fit} and G_F^{dis} obtained from the two procedures previously described are indicated as $\overline{P}_{deb}^{fit}$ and $\overline{P}_{deb}^{dis}$, respectively.

The average value of the experimental loads corresponding to the four points within the range (P_1–P_2) used to determine the fracture energies is taken as P_{deb}, which is also identified as the applied load at point B in Fig. 4a. The values of P_{deb} are provided in Table 2.

The load corresponding to the onset of debonding can also be obtained from Eq. (10):

$$\overline{\overline{P}}_{deb} = \bar{\varepsilon}_{yy} n t^* b^* E \tag{10}$$

where $\bar{\varepsilon}_{yy}$, provided in Table 2 for each test, is the average of the strains measured (not fitted) at the beginning of the bonded area for the four selected points in the range (P_1–P_2) around point B (see Fig. 4a).

Fig. 11 compares the experimental values of P_{deb} with the values of the load $\overline{\overline{P}}_{deb}$, $\overline{P}_{deb}^{fit}$, and $\overline{P}_{deb}^{dis}$, for each specimen instrumented with strain gauges. It should be noted that the values of $\overline{P}_{deb}^{fit}$, and $\overline{P}_{deb}^{dis}$ presented in Fig. 11 are determined using the corresponding average value of the fracture energies provided in Table 2. In general, a good agreement between the average measured load (P_{deb}) and the three values obtained from Eqs. (9) and (10) is observed. Nevertheless, the following factors should be taken into account: (i) for FRCM composites due to the discrete pattern of the bundles, there could be a non-uniform load distribution across the width. For this reason the strain measured in the central bundle of the fiber net may not be the strain at debonding corresponding to the entire applied load, thus leading to a scatter between the load calculated with Eqs. (9) and (10) and the corresponding applied load P_{deb}. (ii) The loads P_{deb}, $\overline{\overline{P}}_{deb}$, $\overline{P}_{deb}^{fit}$, and $\overline{P}_{deb}^{dis}$ are obtained from points in the load response around the assumed position of point B. However the exact position of point B is unknown.

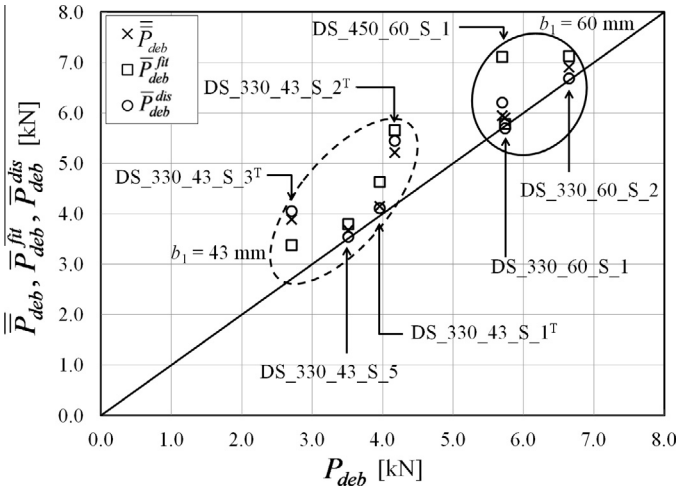

Fig. 11. Comparison between the average measured load (P_{deb}) and the values obtained from Eqs. (9) and (10).

It should be noted that if $\ell > l_{eff}$ the values of P_{deb}, $\overline{\overline{P}}_{deb}$, $\overline{P}^{fit}_{deb}$, and $\overline{P}^{dis}_{deb}$ should vary with the bonded width b_1 but not with the bonded length ℓ because they represent the applied load related to bond and do not include friction. However, the loads in Fig. 11 corresponding to specimens with a bonded width equal to 43 mm or 60 mm are quite scattered. The scatter can be justified by the fact that the load at point B is influenced by the bond quality, which is strongly dependent on the matrix impregnation of the fibers and was not controlled.

For FRP–concrete joints, Chen and Teng [24] proposed a design formula to compute the axial strain corresponding to the load-carrying capacity of the interface when debonding occurs:

$$\bar{\varepsilon}^{FRP}_{yy} = 0.427\beta_L\beta_P\sqrt{\frac{\sqrt{f'_c}}{E_f t_f}} \tag{11}$$

where $\beta_L = 1$ if the bonded length of FRP is greater than the effective bond length. β_P takes into account the effect of the width ratio of the bonded strip to the concrete block [24]. t_f is the nominal thickness of one ply of FRP reinforcement in mm, E_f is elastic modulus of the FRP reinforcement in MPa, and f'_c is the specified compressive strength of concrete in MPa. Similar formulas for the FRP–concrete interface were introduced by several research groups and adopted by international guidelines [44]. The strain at debonding computed with Eq. (11) is lower than the values of $\bar{\varepsilon}_{yy}$ provided in Table 2. As the concrete blocks had two different average compressive strengths, for the shorter blocks (L = 375 mm) Eq. (11) provides a value of 7920 με, whereas for the longer blocks (L = 510 mm) it provides a value of 7460 με. The value of β_P was taken as 1 since a global width effect was not observed, and the value of β_L was taken as 1 since a bonded length greater than 260 mm was considered. It should be noted that Eq. (11) provides a value of the strain at debonding that depends on the compressive strength of concrete. Results presented in this study indicate that Eq. (11) is not applicable to FRCM–concrete joints if debonding occurs at the matrix–fiber interface.

8. Effective bond length

Fig. 12a shows the idealized σ^*–ℓ relation for FRCM–concrete joints proposed by the authors. The dashed line in Fig. 12a shows the σ^*–ℓ relation for FRP–concrete joints when $\ell > l_{eff}$. The ultimate stress increases linearly for bonded lengths greater than l_{eff} due to the contribution of friction. Fig. 12b shows the average of the ultimate stress σ^* for each bonded width tested as a function of the bonded length ℓ for the tests herein presented. Three different bonded widths, namely 34 mm, 60 mm, and 80 mm, corresponding to 4, 7, and 9 bundles, respectively, are considered. The results of the double-lap shear tests published by D'Ambrisi et al. [19] are included for comparison in terms of the average of the ultimate stress σ^* for each bonded width. The results of Fig. 12b resemble the idealized curve of Fig. 12a and show that the ultimate stress σ^* increases as the bonded length ℓ increases up to a value equal to 450 mm. As such, Fig. 12b cannot be used to determine l_{eff} because for $\ell > l_{eff}$, the peak load P^* (and consequently σ^*), as described in Eq. (3), is due to the load associated with both bond and friction. Instead, the effective bond length for FRCM composites should be determined from the strain profiles by considering, for example, points of the load response at the onset of the debonding process as outlined in this paper.

Fig. 12b shows that the average ultimate stress σ^* of specimens with a bonded length of 450 mm is slightly larger than the average ultimate stress σ^* of specimens with a bonded length of 330 mm. The corresponding increase in the ultimate stress $\Delta\sigma^*$ can be calculated by considering the increase in the bonded length ($\Delta\ell$) and the consequent increase of the load carried by friction (Fig. 12a):

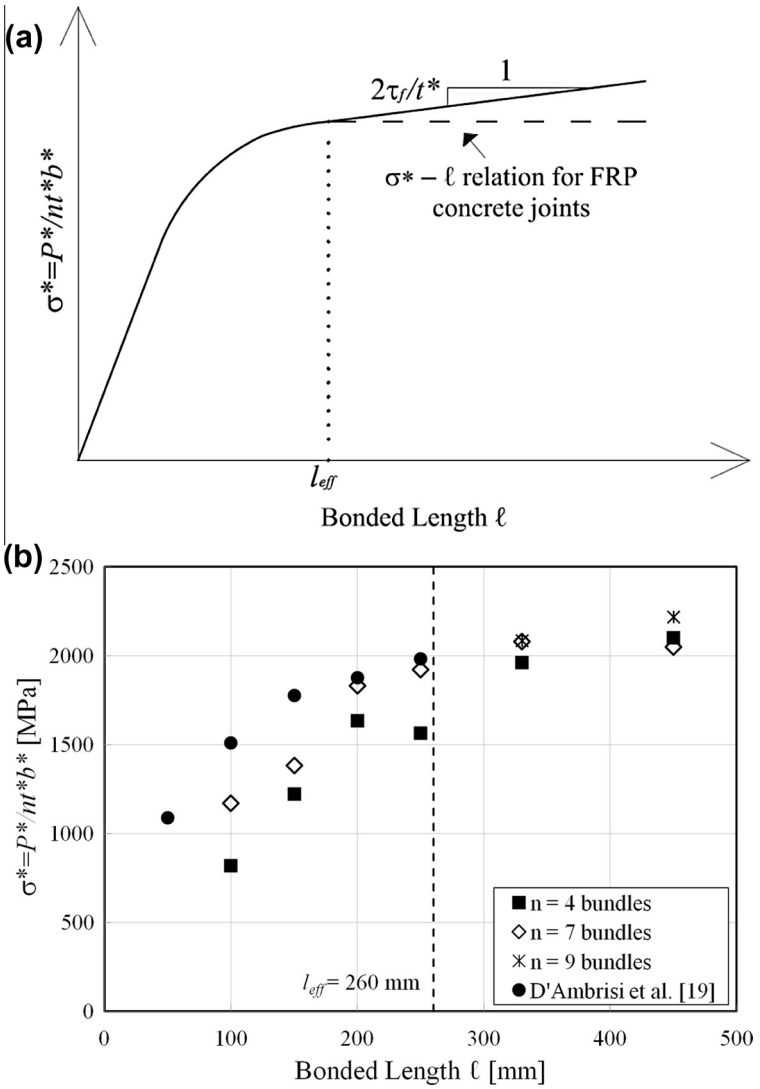

Fig. 12. (a) Idealized ultimate stress σ^* vs. bonded length ℓ curve. (b) Variation of the ultimate stress σ^* as a function of the bonded length ℓ.

$$\Delta\sigma^* = \frac{2\tau_f \Delta\ell}{t^*} \tag{12}$$

The value of $\Delta\sigma^*$ obtained from Eq. (12) is independent of the number of bundles n. Comparing specimens with a bonded length of 450 mm and those with a bonded length of 330 mm ($\Delta\ell$ = 120 mm), Eq. (12) provides a value of $\Delta\sigma^*$ that is consistent with the difference in the average values of σ^* reported in Fig. 12b for ℓ = 330 mm and ℓ = 450 mm. It should be noted, however, that the average values for specimens with 7 bundles and bonded length ℓ = 330 mm and ℓ = 450 mm were very similar.

The effective bond length for the FRP–concrete interface is calculated by [44]:

$$l_{eff}^{FRP} = \sqrt{\frac{n_f t_f E_f}{\sqrt{f_c'}}} \tag{13}$$

where n_f is the number of plies of FRP reinforcement, t_f is the nominal thickness of one ply of FRP reinforcement in mm, E_f is the elastic modulus of the FRP reinforcement in MPa, and f_c' is the specified compressive strength of concrete in MPa. Eq. (13) provides a value of the effective bond length of 54 mm for the shorter blocks (L = 375 mm) and of 57 mm for the longer blocks (L = 510 mm). A formula similar to Eq. (13) was used by Ombres [1] to calculate the effective bond length of the FRCM external reinforcement used to strengthen RC beams. Using this approach, however, the computed effective length in [1] was found to be significantly underestimated. The present study confirms that Eq. (13) should not be used for FRCM composites if the debonding process occurs at the matrix–fiber interface.

It should be noted that the thickness of the fibers used by the authors in Eqs. (11) and (13) is equal to t^*. However, the equivalent thickness of the fibers (0.046 [1,39]), obtained by considering the fibers evenly distributed over the width of the composite, could be used.

9. Conclusions

This paper describes the results of experimental research conducted to study the stress-transfer mechanism at the matrix–fiber interface of fiber reinforced cementitious matrix (FRCM) composites externally bonded to a concrete substrate. Based on the results of this study, the following conclusions can be made:

(1). Debonding occurred at the matrix–fiber interface rather than at the matrix–concrete interface. This is a unique aspect of FRCM composite which indicates that the substrate might not play an important role in the debonding mechanism of this composite. As a consequence, existing formulas included in guidelines used to design FRP strengthening systems cannot be used for FRCM composites due to the different failure modes. Additional studies are necessary to understand the role of the concrete surface treatment and its mechanical properties on the debonding mechanism.

(2). Unlike with FRP–concrete joints, a *global* width effect was not observed with FRCM–concrete joints in terms of the ultimate stress σ^*. This may be due to the independent action of the longitudinal fiber bundles. However it was recognized that a width effect exists within a single fiber bundle due to the different impregnation of the fibers by the matrix.

(3). The load responses showed that after debonding of the fibers from the two layers of matrix occurred, friction contributed to the increase of the applied load. Consequently, the ultimate stress vs. bonded length plot could not be used to determine the effective bond length l_{eff}.

(4). Seven specimens, presented in this paper, were instrumented with strain gauges along the bonded length to study the stress-transfer mechanism and evaluate l_{eff}. It was noticed that the presence of friction altered the strain profile after the onset of debonding. An effective bond length l_{eff} due to bond could be determined from the strain profiles at the onset of debonding. The average l_{eff} was estimated to be 260 mm.

(5). The fracture parameters and in particular the fracture energy associated with bond were determined from the strain profiles of the seven specimens instrumented with strain gauges. The fracture energy and the maximum measured strain at the onset of debonding were used independently to compute the load-carrying capacity associated with initiation of debonding and compare it with the corresponding experimental value of the applied load. The results are in good agreement and confirm that a fracture mechanics approach is suitable to describe the stress transfer at the matrix–fiber interface.

Acknowledgements

The experimental work discussed in this paper was conducted at Missouri University of Science and Technology (Missouri S&T). The authors would like to express their appreciation to the National University Transportation Center (NUTC) at Missouri S&T for providing financial support for this project. Ruredil S.p.A. of San Donato Milanese, Italy, is gratefully acknowledged for providing the composite materials.

References

[1] Ombres L. Debonding analysis of reinforced concrete beams strengthened with fibre reinforced cementitious mortar. Eng Frac Mech 2012;81:94–109.
[2] Wiberg A. Strengthening of concrete beams using cementitious carbon fibre composites. PhD thesis, Royal Institute of Technology, Stockholm, Sweden; 2003.
[3] Banholzer B. Bond behavior of multi-filament yarn embedded in a cementitious matrix, PhD Thesis, RETH Aachen University, United Kingdom; 2004.
[4] Johansson T, Täljsten B. End peeling of mineral based CFRP strengthened concrete structures – A parametric study. In: Proceedings of the international symposium on bond behaviour of FRP in structures (BBFS 2005); 2005. p 197–204.
[5] Triantafillou TC, Papanicolaou CG, Zissinopoulos P, Laourdekis T. Concrete confinement with textile-reinforced mortar jackets. ACI Struct J 2006;103(1):28–37.
[6] Pareek S, Suzuki Y, Kobayashi A. Flexural and shear strengthening of RC beams using newly developed CFRP and Polymer-cement pastes as bonding agents. In: Proceedings of the 8th international symposium on fiber reinforced polymer reinforcement for concrete structures, FRPRCS-8, Patras, Greece, 16–18 July, 2007.
[7] Orosz K, Täljsten B, Fischer G. CFRP strengthening with mineral based composites loaded in shear. In: Proceedings of the 8th international symposium on fiber reinforced polymer reinforcement for concrete structures, FRPRCS-8, Patras, Greece, 16–18 July; 2007.
[8] Täljsten B, Blanksvärd T. Mineral based bonding of carbon FRP to strengthen concrete structures. J Compos Constr, ASCE 2007;11(2):120–8.
[9] Toutanji H, Deng Y. Comparison between organic and inorganic matrices for RC beams strengthened with carbon fiber sheets. J Compos Constr, ASCE 2007;11(5):507–13.
[10] Ombres L. Confinement effectiveness in concrete strengthened with fiber reinforced cement based composite jackets. In: Proceedings of the 8th international symposium on fiber reinforced polymer reinforcement for concrete structures, FRPRCS-8, Patras, Greece, 16–18 July; 2007.
[11] Blanksvärd T. Strengthening of concrete structures by the use of mineral based composites. Licentiate thesis, Luleå Univ. of Technology, Luleå, Sweden; 2007.
[12] Peled A. Confinement of damaged and nondamaged structural concrete with FRP and TRC sleeves. J Compos Constr, ASCE 2007;11(5):514–22.
[13] Hartig J, Häußler-Combe U, Schicktanz K. Influence of bond properties on the tensile behaviour of textile reinforced concrete. Cem Concr Compos 2008;30:898–906.

[14] Bournas DA, Triantafillou TC, Zygouris K, Stavropoulos F. Textile-reinforced mortar versus FRP jacketing in seismic retrofitting of RC columns with continuous or lap-spliced deformed bars. J Compos Constr, ASCE 2009;13(5):360–71.
[15] Blanksvärd T, Täljsten B, Carolin A. Shear strengthening of concrete structures with the use of mineral-based composites. J Compos Constr, ASCE 2009;13(1):25–34.
[16] D'Ambrisi A, Focacci F. Flexural strengthening of RC beams with cement based composites. J Compos Constr, ASCE 2009;15(2):707–20.
[17] Hartig J, Jesse F, Schicktanz K, Häußler-Combe U. Influence of experimental setups on the apparent uniaxial tensile load-bearing capacity of textile reinforcement concrete specimens. Mater Struct, RILEM 2011;45:433–46.
[18] D'Ambrisi A, Feo L, Focacci F. Bond-slip relations for PBO-FRCM materials externally bonded to concrete. Compos – Part B: Eng 2012;43(8):2938–49.
[19] D'Ambrisi A, Feo L, Focacci F. Experimental analysis on bond between PBO-FRCM strengthening materials and concrete. Compos – Part B: Eng 2013;44(1):524–32.
[20] Hashemi S, Al-Mahaidi R. Experimental and finite element analysis of flexural behavior of FRP-strengthened RC beams using cement-based adhesives. Constr Build Mater 2012;26:268–73.
[21] Carloni C, Sneed LH, D'Antino T. Interfacial bond characteristics of fiber reinforced cementitious matrix for external strengthening of reinforced concrete members. In: Proceedings of the 8th international conference on fracture mechanics of concrete and concrete structures (FraMCoS-8), Toledo, Spain, 10–14 March; 2013. p.129–37.
[22] D'Antino T, Sneed LH, Carloni C, Pellegrino C. Bond behavior of the FRCM–concrete interface. In: Proceedings of the 11th international symposium on fiber reinforced polymer reinforcement for concrete structures, FRPRCS-11, Guimaraes, Portugal, 26–28 June; 2013.
[23] Pellegrino C, D'Antino T. Failure due to delamination in concrete elements strengthened with cementitious composites. In: Proceedings of the 8th international conference on fracture mechanics of concrete and concrete structures (FraMCoS-8), Toledo, Spain, 10–14 March, 2013. p.138–43.
[24] Chen JF, Teng JG. Anchorage strength models for FRP and steel plates bonded to concrete. J Struct Eng, ASCE 2001;127(7):784–91.
[25] Wu ZS, Yuan H, Niu H. Stress transfer and fracture propagation in different kinds of adhesive joints. J Eng Mech, ASCE 2002;128(5):562–73.
[26] Yao J, Teng JG, Chen JF. Experimental study on FRP-to-concrete bonded joints. Compos – Part B: Eng 2005;36(2):99–113.
[27] Subramaniam KV, Carloni C, Nobile L. Width effect in the interface fracture during debonding of FRP from concrete. Eng Fract Mech 2007;74:578–94.
[28] Ferracuti B, Savoia M, Mazzotti C. Interface law for FRP–concrete delamination. Compos Struct 2007;80(4):523–31.
[29] Pellegrino C, Tinazzi D, Modena C. An experimental study on bond behavior between concrete and FRP reinforcement. J Compos Constr, ASCE 2008;12(2):180–9.
[30] Subramaniam KV, Carloni C, Nobile L. An understanding of the width effect in FRP–concrete debonding. Strain 2011;47(2):127–37.
[31] Pellegrino C, Modena C. Influence of FRP axial rigidity on FRP–concrete bond behaviour: an analytical study. Adv Struct Eng 2009;12(5):639–49.
[32] Valluzzi MR, Grinzato E, Pellegrino C, Modena C. IR thermography for interface analysis of FRP laminates externally bonded to RC beams. Mater Struct 2009;42(1):25–34.
[33] Salomoni VA, Mazzucco G, Pellegrino C, Majorana CE. Three-dimensional modelling of bond behaviour between concrete and FRP reinforcement. Eng Comput 2011;28(1):5–29.
[34] Achintha M, Burgoyne CJ. Fracture mechanics of plate debonding: validation against experiment. Constr Build Mater 2011;25(6):2961–71.
[35] Carrara P, Ferretti D, Freddi F, Rosati G. Shear tests of carbon fiber plates bonded to concrete with control of snap-back. Eng Fract Mech 2011;78(15):2663–78.
[36] Grace C, Yang Y, Sneed LH. Fracture mechanics approach to predicting the behavior of reinforced concrete members with externally-bonded fiber reinforced polymer laminates. SP-286, ACI; 2012, 7-1-7-20.
[37] Carloni C, Subramaniam KV. Application of fracture mechanics to debonding of FRP from RC members. SP-286, ACI; 2012,10-1-10-14.
[38] Carrara P, Ferretti D. A finite difference model with mixed interface laws for shear tests of FRP plates bonded to concrete. Compos – Part B: Eng 2013;54:329–42.
[39] Ruredil. X mesh gold data sheet. Ruredil S.p.A. 2009, Milan, Italy. <http://english.ruredil.it/SchedeProdottoENG/RuredilXMeshGOLD_ing_1.pdf>.
[40] ASTM. Standard test method for compressive strength for cylindrical concrete specimens. C39/C39M-12, ASTM International 2011, 7 pages.
[41] ASTM. Standard test method for splitting tensile strength of cylindrical concrete specimens. C496/C496M ASTM International 2011, 5 pages.
[42] ASTM. Standard test method for tensile properties of polymer matrix composite materials. D3039/D3039M, ASTM International 1996, 6 pages.
[43] Toyobo. Zylon© (PBO fiber) technical information. Toyobo Co 2005, Ltd., Osaka, Japan. <http://www.toyobo-global.com/seihin/kc/pbo/Technical_Information_2005.pdf>.
[44] ACI 440.2R. Guide for the design and construction of externally bonded FRP systems for strengthening concrete structures. American Concrete Institute; 2008.